Superconducting properties of $MoTe_2$ from *ab initio* anisotropic Migdal-Eliashberg theory

Hari Paudyal,[1] Samuel Poncé,[2,3] Feliciano Giustino,[4,5] and Elena R. Margine[1,*]

[1]*Department of Physics, Applied Physics, and Astronomy, Binghamton University-SUNY, Binghamton, New York 13902, USA*
[2]*Department of Materials, University of Oxford, Parks Road, Oxford OX1 3PH, United Kingdom*
[3]*Theory and Simulation of Materials (THEOS), École Polytechnique Fédérale de Lausanne, CH-1015 Lausanne, Switzerland*
[4]*Oden Institute for Computational Engineering and Sciences, The University of Texas at Austin, Austin, Texas 78712, USA*
[5]*Department of Physics, The University of Texas at Austin, Austin, Texas 78712, USA*

(Received 10 December 2019; revised manuscript received 26 May 2020; accepted 1 June 2020; published 11 June 2020)

Molybdenum ditelluride ($MoTe_2$) is attracting considerable interest since it is the archetypal type-II Weyl semimetal and a candidate for topological superconductivity. We investigate the superconducting phase diagram of two $MoTe_2$ polymorphs using the *ab initio* anisotropic Migdal-Eliashberg theory, and we show that the superconducting dome originates from the synergistic contribution of the density of states at the Fermi level and the transverse acoustic Te modes in the $1T'$ phase. We find that the electron and hole pockets carry trivial s-wave order parameters of slightly different magnitude, reminiscent of a two-gap structure as suggested by recent experiments. We suggest that a possible route for enhancing the superconducting critical temperature, and realizing s_{+-} pairing, in the T_d phase is to exploit its nontrivial band topology via electron doping.

DOI: 10.1103/PhysRevB.101.214515

I. INTRODUCTION

Molybdenum ditelluride ($MoTe_2$) is a member of the transition metal dichalcogenide family that has recently attracted significant attention since it hosts a wealth of exotic phases and emergent phenomena. Similar to the sister compound tungsten ditelluride (WTe_2) [1–3], $MoTe_2$ displays large nonsaturating magnetoresistance [4–6] and pressure-driven superconductivity [7–11], and it is predicted to be a type-II Weyl semimetal [12–16]. Since $MoTe_2$ is a prime candidate for realizing topological superconductivity and Marjorana fermions [10,11,17–20], it is important to understand the interplay between the superconducting pairing mechanism, the Fermi surface (FS) topology, and the structural phase transition under applied pressure.

The observed domelike shape of the superconducting critical temperature (T_c) with pressure and chemical doping has been associated with the structural transition from the noncentrosymmetric T_d phase to the centrosymmetric $1T'$ phase [5,7–10,17,21–23] shown in Fig. 1(a), but several open questions remain: What is the nature of the superconducting gap in the two phases? Can the topological states take part in and enhance the superconducting paring in the T_d phase? How does the critical temperature change when the Fermi level crosses a Weyl point?

Resistivity measurements have revealed that the T_c first increases sharply from 0.1 K at ambient pressure to approximately 5 K at pressures below 1 GPa, and then follows a gradual increase before reaching the maximum value of $T_c = 8.2$ K at 11.7 GPa [7]. Since the T_d-to-$1T'$ phase transition is suppressed at a critical pressure (P_c) between 1.5 and 4 GPa, this two-stage behavior was attributed to superconductivity in the T_d and $1T'$ phases, respectively [7]. In contrast, three subsequent transport studies have found a much lower critical pressure for the structural phase transition, and established the coexistence of the two phases at low temperature in the vicinity of P_c as well as a strong superconductivity enhancement in the phase transition region [5,8,9]. Takahashi *et al.* observed no evidence of the T_d phase at 0.75 GPa down to 0 K [8], Heikes *et al.* reported the suppression of the T_d phase below 80 K at 0.82 GPa [9], and Lee *et al.* found that the structural transition temperature decreases to 58 K at 1.1 GPa, with no signature of the T_d phase above 1.4 GPa [5]. The existence of a mixed phase region has been further supported by neutron-diffraction experiments, which have shown a $30 \pm 5\%$ volume fraction of the T_d phase present at 1 GPa [9] and even evidence of the emergence of a new centrosymmetric T_d^* phase across the T_d-$1T'$ phase boundary [11].

Recent experiments have probed the nature of the superconducting gap in this system. Two isotropic s-wave superconducting gaps have been determined from muon-spin rotation experiments of $MoTe_2$ under pressure [10] and specific heat measurements of S-doped $MoTe_{2-x}S_x$ ($x \sim 0.2$) [17]. A two-band model has also been used to explain the superconducting properties in Se-substituted $MoTe_2$ thin films [24]. In order to make progress toward topological superconductivity, it is paramount to understand the origin of the superconducting dome in this compound, and to clarify the nature of the order parameter.

Here we analyze the nature of the superconducting dome and the pairing mechanism in $MoTe_2$ using the *ab initio* anisotropic Migdal-Eliashberg (ME) theory [25,26]. We demonstrate that the ME theory reproduces quantitatively the measured superconducting dome, and we attribute the pressure dependence of the critical temperature to the nonlinear

*rmargine@binghamton.edu

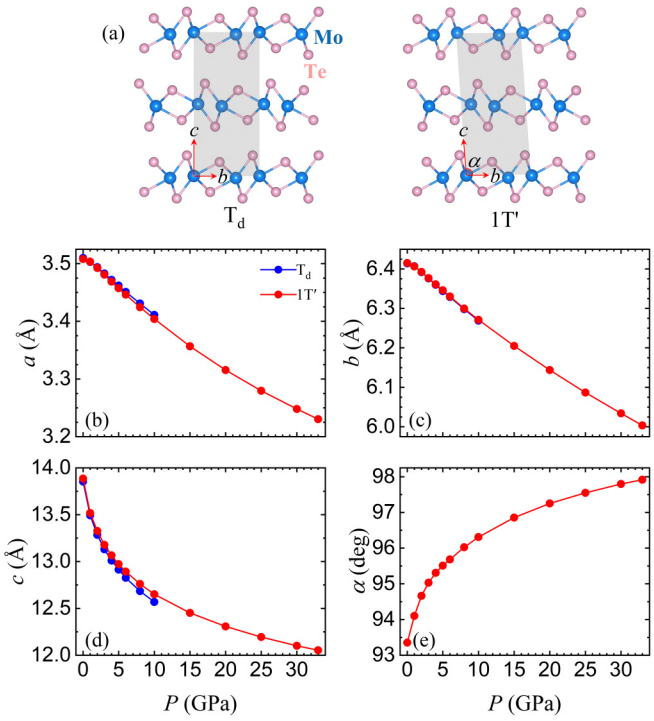

FIG. 1. (a) Crystal structures of $MoTe_2$ in the T_d and $1T'$ phases. (b)–(e) Pressure dependence of the structural parameters for the T_d (blue symbols) and $1T'$ (red symbols) phases.

variation of the transverse acoustic Te modes with compression. We show that the system exhibits *s*-wave pairing and an anisotropic gap structure that is reminiscent of a two-gap scenario, in line with recent experiments.

II. METHODS

The *ab initio* calculations were carried out with the QUANTUM ESPRESSO [27] package. We employed relativistic norm-conserving pseudopotentials [28] with the Perdew-Burke-Ernzerhof [29] exchange-correlation functional in the generalized gradient approximation, where the Mo $4d^5 5s^1$ and Te $5p^4 5s^2$ orbitals were included as valence electrons. To properly treat the long-range dispersive interactions, we used the nonlocal van der Waals (vdW) density functional optB86b-vdW [30,31]. A plane-wave kinetic-energy cutoff value of 60 Ry, a Γ-centered $12 \times 6 \times 4$ Monkhorst-Pack **k** mesh [32], and a Methfessel and Paxton smearing [33] width of 0.02 Ry were used for the Brillouin-zone (BZ) integration. The atomic positions and lattice parameters were optimized until the self-consistent energy was converged within 2.7×10^{-5} eV and the maximum Hellmann-Feynman force on each atom was less than 0.005 eV/Å. For density of states and Fermi surface calculations, we used denser meshes of $24 \times 12 \times 8$ and $60 \times 40 \times 20$, respectively. The dynamical matrices and the linear variation of the self-consistent potential were calculated within density-functional perturbation theory [34] on the irreducible set of a regular $4 \times 4 \times 3$ **q** mesh.

The isotropic and anisotropic Migdal-Eliashberg (ME) formalism [25,26] was used to investigate the superconducting properties with the EPW code [35,36]. To obtain the electron-phonon matrix elements on dense grids we use Wannier interpolation [37,38] on a uniform Γ-centered $8 \times 8 \times 3$ grid. Forty-four maximally localized Wannier functions (five *d* orbitals for each Mo atom and three *p* orbitals for each Te atom) were used to describe the electronic structure near the Fermi level (E_F). Uniform $56 \times 32 \times 16$ **k**-point and $28 \times 16 \times 8$ **q**-point grids and an effective Coulomb potential $\mu^* = 0.1$ were used for solving the anisotropic ME equations. The Matsubara frequency cutoff was set to 0.2 eV and the Dirac deltas were replaced by Lorentzians of width 50 meV (electrons) and 0.1 meV (phonons).

III. CRYSTAL STRUCTURE

$MoTe_2$ crystallizes in three different phases: hexagonal-2H structure (α phase, space group $P6_3/mmc$, No. 194), monoclinic-$1T'$ (β-phase, space group $P2_1/m$, No. 11), and orthorhombic-T_d (γ phase, space group $Pmn2_1$, No. 31). While both the semiconducting 2H and the semimetallic $1T'$ structures are stable at room temperature and ambient pressure, the semimetallic T_d phase with broken inversion symmetry can be stabilized by cooling the $1T'$ phase down to approximately 250 K [7]. In this work, we will focus on the semimetallic T_d and $1T'$ phases. As shown in Fig. 1(a), the two phases are closely related, both having a unit cell made of two Te-Mo-Te sandwiches and sharing the same in-plane crystal structure. A first-order phase transition between the T_d and $1T'$ phase can be achieved by a slight relative sliding of the Te-Mo-Te layers. This structural transformation causes a small change in the vertical stacking, tilting the angle between the *b* and *c* lattice vectors in the $1T'$ unit cell.

At zero pressure, the calculated structural parameters are $a = 3.510$ Å, $b = 6.414$ Å, $c = 13.855$ Å for T_d, and $a = 3.508$ Å, $b = 6.415$ Å, $c = 13.886$ Å, $\alpha = 93.35°$ for $1T'$, respectively. For comparison, the experimental lattice parameters at ambient pressure are $a = 3.477$ Å, $b = 6.335$ Å, $c = 13.889$ Å for the T_d phase [7], and $a = 3.469$ Å, $b = 6.320$ Å, $c = 13.860$ Å, $\alpha = 93.917°$ for the $1T'$ phase [39]. Under compression, the in-plane lattice constants *a* and *b* decrease monotonically, while the out-of-plane lattice constant *c* first drops sharply before beginning a slower descent around 5 GPa as shown in Figs. 1(b)–1(d). A gradual increase of the angle α with pressure can also be seen in Fig. 1(e) for the $1T'$ phase. All these results are in good agreement with experimental and theoretical data reported in the literature [7,9,10].

IV. RESULTS

Figures 2(a)–2(g) show the electronic structure of the T_d and $1T'$ phases at 0 GPa with the inclusion of spin-orbit coupling (SOC). At 0 GPa, both structures display hole and electron bands crossing the Fermi level (E_F) along the Y-Γ-X direction. These bands give rise to a multisheet FS consisting of (i) a butterflylike hole pocket (FS1) enclosing a smaller ellipsoidal hole pocket (FS2) centered at Γ, and (ii) a two-dimensional (2D) electron pocket (FS3) surrounding a second 2D electron pocket (FS4) distributed along the *z* axis. While in the $1T'$ phase the electron and hole pockets are doubly degenerate, in the T_d phase the degeneracy is removed due to the broken inversion symmetry and each pocket is split

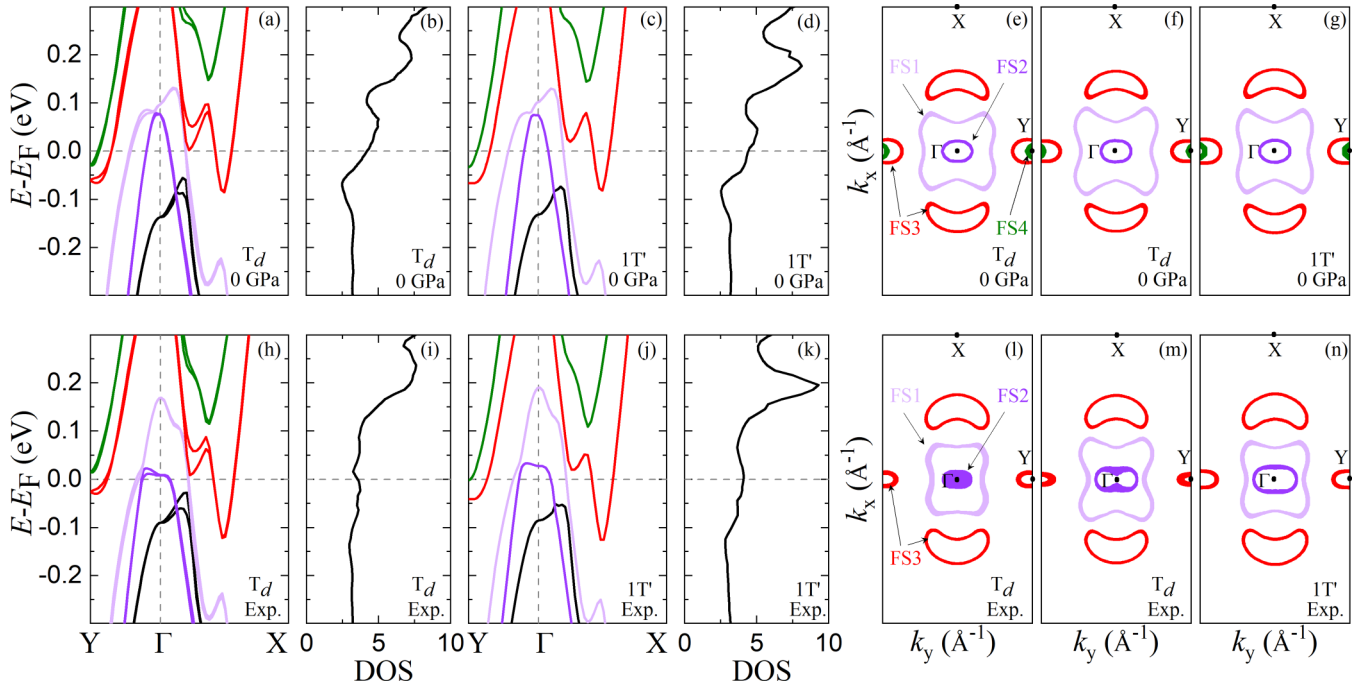

FIG. 2. Top row: Calculated (a)–(d) electronic band structure and density of states (DOS) in states/eV/u.c., and (e)–(g) cross section of the Fermi surfaces in the Γ-X-Y plane for the T_d and 1T' phases at 0 GPa. A finite splitting of the bands can be observed in the T_d phase due to the combined effect of SOC and the lack of inversion symmetry [each pair of bands is shown with the same color in panel (a)]. The corresponding pairs of inner and outer FS sheets are shown in the (e) and (f) panels. The holelike bands (light- and dark-purple curves) give rise to the Γ-centered FS1 and FS2 hole pockets, while the electronlike bands (red and green curves) give rise to the FS3 and FS4 electron pockets. Bottom row: Same plots as in the top row but at the experimental unit cell parameters at ambient pressure.

into a pair of sheets as shown in Figs. 2(a) and 2(h). This is a manifestation of the Rashba-Dresselhaus effect, as can be seen near the band extrema at the Y and Γ points. This effect is most noticeable for the minor electron band above the Fermi level along the Γ-X direction where a splitting of approximately 47 meV is observed [bands shown in red in Fig. 2(a)].

Results at higher pressures are shown in Supplemental Figs. S1– S4 [40]. As pressure increases, the bands shift relative to E_F and the difference in the FS between the two phases becomes more pronounced. For instance, at 4 GPa, the minor electron pocket along the Γ-X direction shrinks in T_d, while it spreads out and touches the outer hole pocket in 1T'. Later we show how these changes in the electronic structure with applied pressure play an important role in the superconducting properties of the two phases.

The vibrational spectra and the phonon density of states (PHDOS) in the T_d and 1T' phases at 0 GPa are shown in Figs. 3(a), 3(b), 3(d), and 3(e). The results at 0 GPa are in good agreement with experimental and theoretical results available in the literature [9,41–44] (see Supplemental Table S1 [40]). To assess the importance of the SOC, we also calculated the phonon frequencies at specific high-symmetry points and, similar to a previous report [9], we found the effect to be negligible [see solid red symbols in Figs. 3(a) and 3(d)]. The two phases exhibit very similar phonon dispersions, and three energy regions can be distinguished with predominant contributions stemming from the in-plane Te_{xy} vibrations (below 20 meV), the in-plane Mo_{xy} vibrations (20–30 meV), and the out-of-plane Mo_z vibrations (above 30 meV) as shown in Figs. 3(b) and 3(e).

With increasing pressure, all phonon modes harden across the whole BZ (see Supplemental Figs. S5 and S6 [40]) with the exception of the lowest-energy branch along the X-S direction which softens at low pressures in the 1T' phase [see Fig. 4(a)]. This transverse acoustic (TA) phonon mode is mainly characterized by displacements of Te atoms in both phases as illustrated in Supplemental Fig. S7 [40]. A similar softening of the low-energy TA branch has been recently uncovered not only in the 1T' phase of $MoTe_2$ [45] but also in that of the sister compound WTe_2 [46].

In order to clarify the nature of the electron-phonon coupling (EPC) in $MoTe_2$, we begin by examining the isotropic Eliashberg spectral function $\alpha^2F(\omega)$ and the cumulative EPC strength $\lambda(\omega)$. The results at 0 GPa are plotted in Figs. 3(c) and 3(f), while those at higher pressures can be found in Supplemental Figs. S5 and S6 [40]. A comparison of the $\alpha^2F(\omega)$ with the PHDOS indicates that there is an increased coupling to the Te vibrational modes below 20 meV in both phases. The breakdown of the EPC strength into contributions arising from the low- and high-energy phonons demonstrates that at 0 GPa almost 80% of the total coupling comes from the Te modes. Figure 4(c) summarizes the dependence of λ as a function of pressure. In the T_d phase, λ decreases with the applied pressure as the phonon modes harden and the density of states at the Fermi level (N_F) decreases. In contrast, in the 1T' phase, λ displays a dome-shaped variation and peaks between 6 and 8 GPa. This dependence correlates closely with

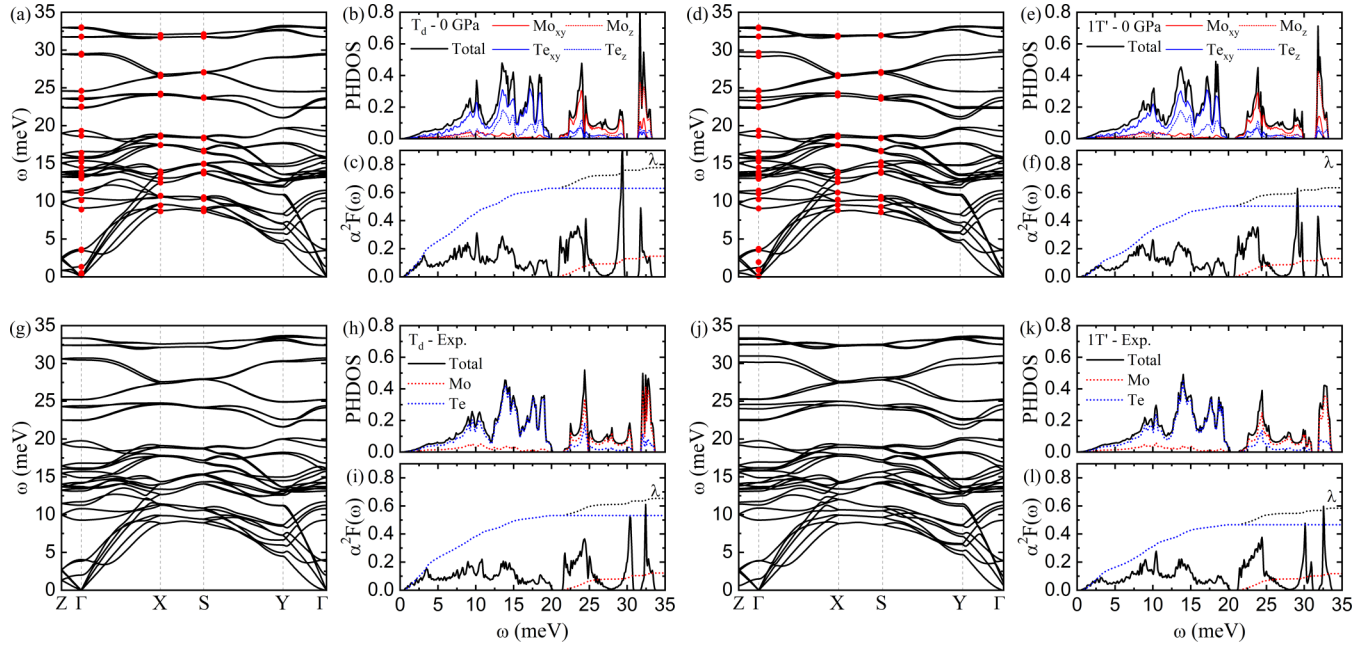

FIG. 3. Top row: Calculated (a),(d) phonon dispersion, (b),(e) phonon density of states (PHDOS), (c),(f) isotropic Eliashberg spectral function $\alpha^2F(\omega)$, electron-phonon coupling strength $\lambda(\omega)$ for the T_d and $1T'$ phases at 0 GPa. The total PHDOS (black line) is decomposed with respect to the in-plane and out-of-plane vibrations of the Mo and Te atoms. The total electron-phonon coupling strength (dotted black line) is decomposed with respect to the vibrations of the Mo (red lines) and Te (blue lines) atoms. The solid symbols represent the phonon frequencies calculated with spin-orbit coupling. Bottom row: Same plots as in the top row but at the experimental unit cell parameters at ambient pressure.

the behavior of N_F and the low-energy modes in the 6–9 meV range along the X-S direction. As shown in Figs. 4(a) and 4(b) and also reported previously [45], the two exhibit an almost mirrored dependence over the full pressure range, which leads to their cooperative effect to λ. The low-energy TA mode

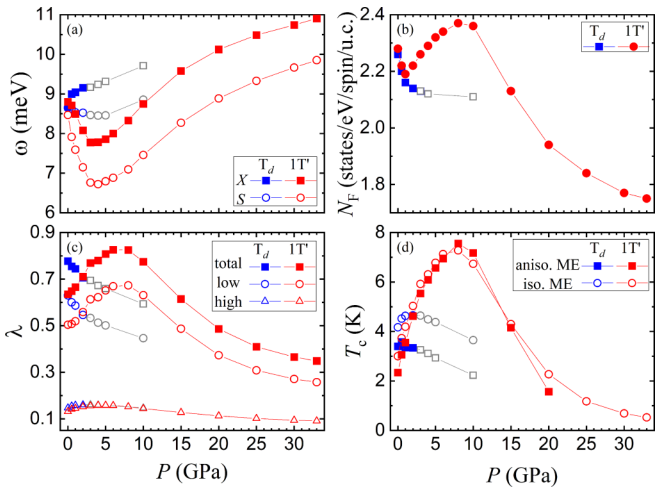

FIG. 4. Variation with pressure of the (a) low-energy TA mode at X and S, (b) N_F, (c) λ, and (d) T_c for the T_d (blue) and $1T'$ (red) phases, respectively. In (c), squares represent the total λ, and circles and triangles represent the contribution of the low- and high-energy modes. In (d), squares and circles represent the T_c obtained from the numerical solutions of the anisotropic and isotropic ME equations. The data points in the pressure region where the T_d phase is experimentally known to be suppressed are shown in gray.

was also found to have a significant contribution to λ in the $1T'$ phase of WTe_2 [46]. In contrast to our results and those from Refs. [45,46], Heikes *et al.* [9] observed no phonon softening in the $1T'$ phase of $MoTe_2$ up to 10 GPa. As a result, the estimated λ was found to have a similar strength and to decrease slightly with pressure in both phases, giving an opposite trend for the T_c versus pressure behavior as compared to the one observed experimentally [9].

To gain more insight into the superconductivity of $MoTe_2$, we compute the superconducting gap function $\Delta_{\mathbf{k}}$ on the FS by solving the anisotropic ME equations [25,26,36]. As shown in Fig. 5, we find that a continuous anisotropic gap develops on the FS. Although we do not find definitive evidence of a two-gap structure, we observe that the distribution of the superconducting gap on the electron and hole Fermi pockets peak at slightly different energies (see rectangle in Supplemental Figs. S3 and S4 [40]). In particular, while the superconducting gap Δ_1 associated with the electron sheets FS3 and FS4 spreads over the full range of the energy distribution of the Δ_2 gap associated with the hole sheets FS1 and FS2 [red and blue lines in Figs. 6(a) and 6(d)], we also see that Δ_1 is mostly concentrated in the upper half of the energy gap distribution and has a pronounced peak near the maximum of $\Delta_{\mathbf{k}}$.

As the pressure is increased to 5 GPa, the anisotropic structure of the superconducting gap in the T_d phase is only slightly affected, both Δ_1 and Δ_2 gaps continuing to overlap over the full bandwidth of $\Delta_{\mathbf{k}}$ [Fig. 6(b)]. In contrast, the energy distribution of the superconducting gap in the $1T'$ phase undergoes substantial changes as the hole and electron pockets spread out more and start to merge [Fig. 6(e)]. The

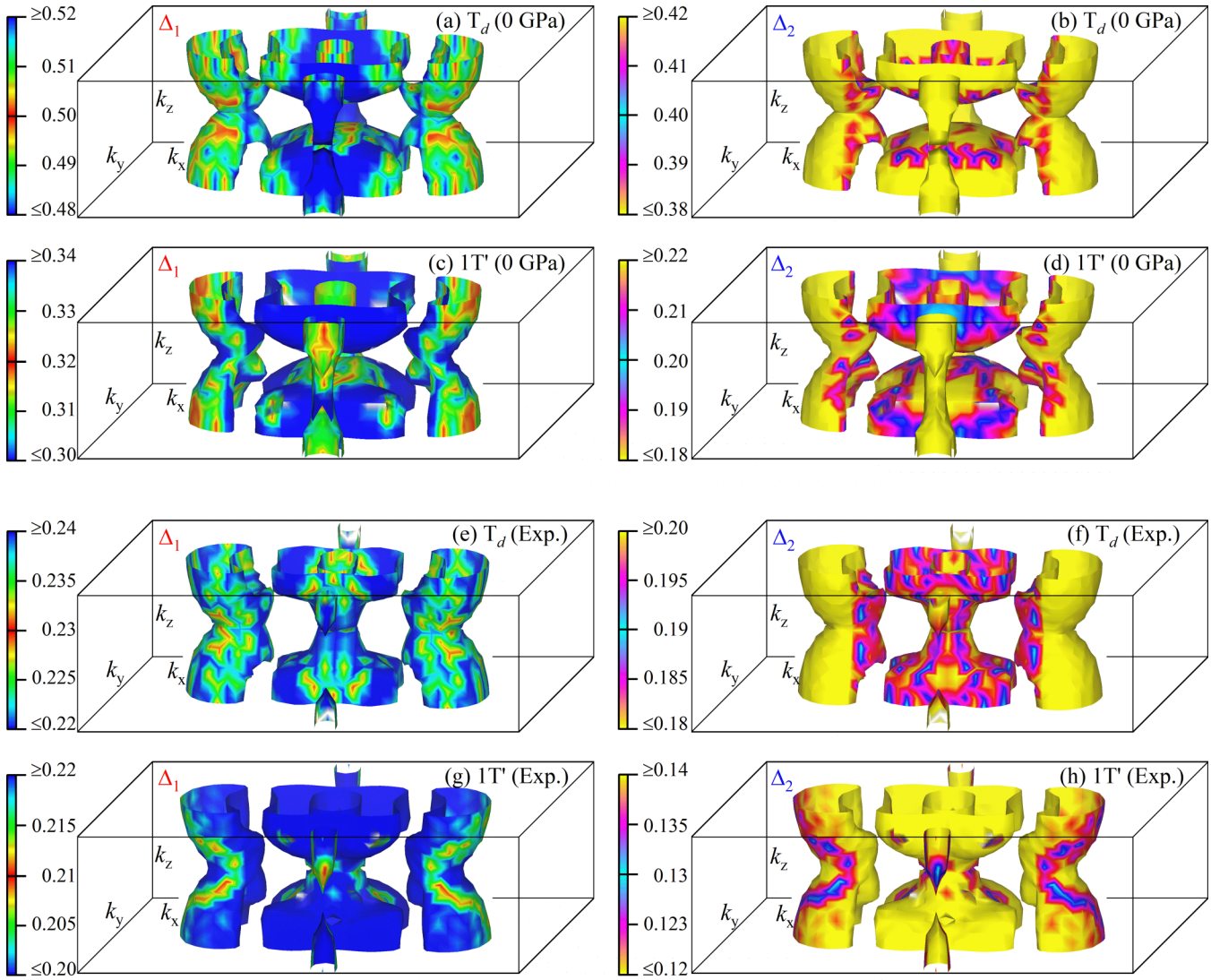

FIG. 5. Momentum-resolved superconducting gap $\Delta_{\mathbf{k}}$ (in meV) on the Fermi surface [47] at 0.5 K for the T_d and $1T'$ phases (a)–(d) at 0 GPa and (e)–(h) at the experimental lattice constants at ambient pressure. The distribution of the electronic states on the Fermi surface contributing the most to the Δ_1 and Δ_2 gaps is color-coded with Gaussians peaked at (a) 0.50 meV, (b) 0.40 meV, (c) 0.32 meV, and (d) 0.20 meV; (e) 0.23 meV, (f) 0.19 meV, (g) 0.21 meV, and (h) 0.13 meV. The ranges of the color maps correspond to the Δ_1 and Δ_2 gaps indicated in Figs. 6(a) and 6(d) at 0 GPa and Figs. 6(c) and 6(f) at the experimental lattice constants at ambient pressure for the T_d and $1T'$ phases.

anisotropy in the $1T'$ phase becomes so pronounced that at 5 GPa the energy distribution of the gap is four times larger than that at 0 GPa. Above 10 GPa the spread in $\Delta_{\mathbf{k}}$ decreases; at 20 GPa the bandwidth being again comparable to the one found at zero pressure (see Supplemental Figs. S8 and S9 [40]). Another noticeable pressure-dependent characteristic is the narrowing of the energy profile of Δ_2 with respect to Δ_1 and its shift toward the lower-energy region of $\Delta_{\mathbf{k}}$.

Several studies have pointed out that the electronic structure of $MoTe_2$ is highly sensitive to the crystal structure parameters [6,16,45,49,50], therefore it is important to examine the sensitivity of our results to small changes in the lattice constants. To this aim, we calculated the superconducting gap at the experimental unit cell parameters at ambient pressure while allowing the atomic positions to relax [40]. The resulting electronic structure and phonon dispersion are shown in Figs. 2(h)–2(n) and Figs. 3(g)–3(l). While the phonon frequencies are largely unaffected, we observe that the hole and electron bands shift down/up in energy relative to E_F, respectively, by as much as 70 meV. These changes in the FS topology lead to a markedly narrower distribution of the superconducting gap [see Figs. 6(c) and 6(f)]. This time, although the gaps Δ_1 and Δ_2 associated with the electron and hole FS sheets overlap in energy, we can see two peaks at $\Delta_1 = 0.23$ meV and $\Delta_2 = 0.20$ meV in T_d, and $\Delta_1 = 0.21$ meV and $\Delta_2 = 0.13$ meV in $1T'$, respectively. These results are in line with magnetic penetration depth measurements of $MoTe_2$ at 0.45 GPa [10] and specific heat measurements of S-doped $MoTe_{2-x}S$ ($x \sim 0.2$) [17].

The numerical solutions to the ME equations give T_c values that are in overall good agreement with the experimental measurements as shown in Fig. 7. While the critical temperature in the T_d phase remains nearly constant under compression, in the $1T'$ phase it shows an almost fourfold increase, yielding a

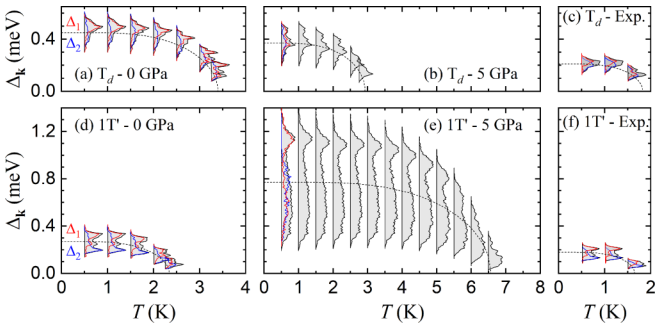

FIG. 6. Energy distribution of the superconducting gap $\Delta_{\mathbf{k}}$ as a function of temperature for the T_d (top panels) and $1T'$ (bottom panels) phases at 0 GPa, 5 GPa, and experimental lattice parameters at ambient pressure. The red and blue curves represent contributions to the Δ_1 and Δ_2 superconducting gaps associated with the electron and hole FS sheets, respectively. The dashed lines are fits obtained by solving numerically the BCS gap equation [48] using the average Δ_0 and T_c from our first-principles calculations.

maximum value of 7.6 K at 8 GPa. This increase in T_c provides evidence for a phonon-driven superconducting mechanism, and confirms that the $1T'$ phase is responsible for the sharp increase in the critical temperature observed experimentally at moderate pressures. By further analyzing the variation of the T_c and EPC strength λ with pressure [see Figs. 4(c) and 4(d)], we find that the domelike shape superconducting phase diagram of $MoTe_2$ comes from the synergistic contribution of the density of state at the Fermi level N_F and the TA mode in the $1T'$ phase.

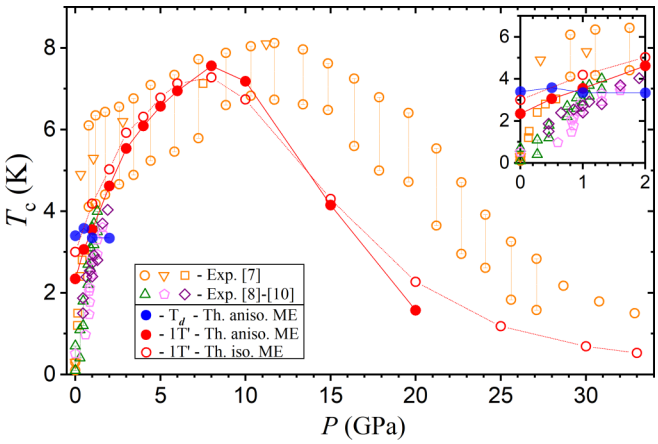

FIG. 7. Comparison between experimental and theoretical results for T_c as a function of pressure. The experimental data are from Ref. [7] (orange circles and triangles from electrical resistivity and orange squares from magnetization measurements), Ref. [8] (green triangles from electrical resistivity measurements), Ref. [9] (magenta pentagons from neutron-scattering measurements), and Ref. [10] (purple diamonds from AC-susceptibility measurements). The blue and red symbols represent the theoretical data for the T_d and $1T'$ phases. For $1T'$, the filled and open red circles represent the solutions of the anisotropic and isotropic ME equations (above 20 GPa the gap is too small to be resolved at the anisotropic level). The vertical lines are a guide to the eye for differences in onset and zero-resistivity T_c in experimental data at various pressures.

We further explore how to take advantage of the Weyl and Rashba-split states in the T_d phase to achieve a superconducting system with nontrivial FS topology. At the experimental lattice constants, the Weyl nodes are found at the intersection of electron and hole pockets 17 meV (W_1) and 65 meV (W_2) above the E_F [Figs. 8(a) and 8(b)], in agreement with previous studies [11,12,50]. As shown in Figs. 8(c)–8(e), moving E_F at the Weyl points or inside the Rashba-split bands changes the Fermi surface, with the most substantial effect at the W_2 point where the inner hole and electron pocket FS2 and FS4 disappears and appears, respectively. As a result, for the W_2 point, there is an almost 10% enhancement in the EPC strength due to the increased coupling of the high-energy Mo modes and a wider distribution of the superconducting gap which resides almost entirely on the electron pockets FS3 and FS4 as shown in Figs. 8(f)–8(j). Considering that the four W_2 points occur in pairs with opposite chirality, the electron-doped system provides the necessary condition for realizing nontrivial sign-changing s_{+-} pairing [20].

V. DISCUSSION

We now comment on the difference between the calculated and measured critical temperature. Despite an overall good agreement between the theoretical and experimental results as shown in Fig. 7, the T_c, in particular at 0 GPa, is largely overestimated. In fact, an important question that remains open is why first-principles calculations systematically tend to overestimate the critical temperature and zero-temperature superconducting gap in transition metal dichalcogenides [52–55]. In $MoTe_2$, we find that the critical temperature is reduced by about a factor of 2 if we consider the superconducting gap calculated at the experimental lattice parameters. In this case, we obtain T_c values of 1.7 K for T_d and 1.6 K for $1T'$, which compare well with the 1.5 and 1.33 K values at 0 GPa found in previous theoretical calculations [9]. These results highlight the fact that small variations in the lattice parameters lead to appreciable changes in the electronic structure near the Fermi level which can then substantially affect the superconducting gap and critical temperature. Additional calculations in Supplemental Fig. S10 [40] also show how the variation in N_F can have a significant impact on the calculated T_c due to its direct effect on the EPC strength λ. However, all these differences alone cannot entirely account for the observed discrepancy with experiment.

Strong electron-electron interactions and spin fluctuations have been shown to considerably reduce the T_c when included alongside the electron-phonon interactions. For instance, for doped MoS_2 thin flake and bulk $TiSe_2$, the T_c was reduced by about a factor of 2 [56] and for FeB_4 by a factor of 25 [57] to reach the experimental values. To investigate the effect of an enhanced Coulomb repulsion between the Cooper-pair electrons, we calculated the dependence of T_c on the Coulomb pseudopotential μ^* as shown in Supplemental Fig. S11. This analysis shows that to match the experimental T_c very different values of μ^* are required in the low, central, and high pressure regions. For instance, a value $\geqslant 0.3$ is estimated at 0 GPa and the experimental lattice parameters at ambient pressure, well beyond the common range of 0.1–0.2. These results highlight the limitation of using a single constant μ^*

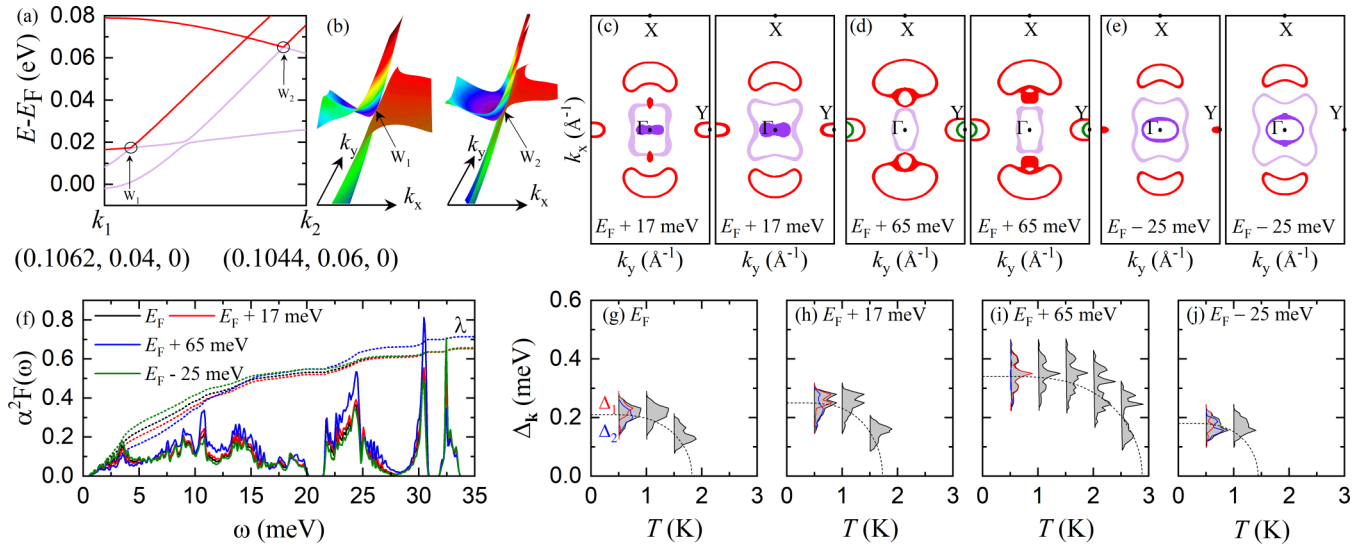

FIG. 8. (a),(b) Band structure and energy isosurfaces revealing the Weyl points W_1 and W_2 at the intersections of electron and hole pockets. W_1 (chirality +1) and W_2 (chirality −1) lie 17 and 65 meV above the Fermi level. The coordinates of the Weyl points are $W_1 = (0.10599, 0.01028, 0)\ \frac{2\pi}{a}$ and $W_2 = (0.10463, 0.05305, 0)\ \frac{2\pi}{a}$. Cross section of the Fermi surfaces in the Γ-X-Y plane calculated by shifting the Fermi level at the position of (c) W_1 ($E_F + 17$ meV), (d) W_2 ($E_F + 65$ meV), and (e) Rashba-split states ($E_F - 25$ meV). (f) Eliashberg spectral function $\alpha^2F(\omega)$ and EPC strength $\lambda(\omega)$. Energy distribution of the superconducting gap $\Delta_{\mathbf{k}}$ as a function of temperature calculated at (g) the Fermi level and by shifting the Fermi level at the position of (h) W_1 ($E_F + 17$ meV), (i) W_2 ($E_F + 65$ meV), and (j) Rashba-split states ($E_F - 25$ meV). All calculations were performed for the T_d phase at the experimental lattice constants at ambient pressure. The position, chirality, and energy isosurface of the Weyl points were obtained with the WANNIERTOOLS package [51].

parameter which could be overcome by computing the state-dependent electron-electron repulsion, as done, for example, in Refs. [54,58–60].

Finally, the compilation of the experimental T_c data in Fig. 7 illustrates that (i) the values reported in various studies for the low pressure region can differ by as much as a factor of 3, and (ii) there are substantial differences observed between the onset and zero resistance T_c (see, for instance, the data from Ref. [7] shown as orange circles). Nonhydrostatic pressure conditions in the experimental setup, the coexistence of mixed phases, and the presence of phase inhomogeneities can, in principle, change the T_c considerably. This can explain, as for other superconductors [53,61,62], part of the discrepancy between different experiments as well as between experiments and theory. Therefore, further theoretical analysis combined with experimental measurements of superconducting properties are needed to better understand the dome-shaped superconducting diagram over the full pressure range.

VI. CONCLUSIONS

We employed the *ab initio* anisotropic Migdal-Eliashberg theory to elucidate the nature of the superconducting paring mechanism in the T_d and $1T'$ phases of $MoTe_2$. We show that the origin of the superconducting dome lies in the synergistic contribution of the density of states at the Fermi level and the TA mode frequency with pressure in the $1T'$ phase. Our calculations provide evidence for *s*-wave superconductivity in both phases, and the energy distribution of the order parameter is reminiscent of a two-gap scenario, although clearly disconnected superconducting gaps could not be identified. Based on our findings, the contribution of nontrivial states at the Weyl points can enhance the critical temperature, and possibly induce nonconventional pairing, in the noncentrosymmetric T_d phase. This could be achieved by slightly moving up Fermi level via electron doping [17,20,24].

ACKNOWLEDGMENTS

H.P. and E.R.M. acknowledge support from the National Science Foundation (Award No. OAC–1740263) and Binghamton University High Performance (SPIEDIE) Computing. This work used the Extreme Science and Engineering Discovery Environment (XSEDE) [63], which is supported by National Science Foundation Grant No. ACI-1548562. Specifically, this work used Comet at the San Diego Supercomputer Center through allocations TG-DMR180047 and TG-DMR180071. S.P. acknowledges support from the Leverhulme Trust (Grant No. RL-2012-001) and from the European Unions Horizon 2020 Research and Innovation Programme, under the Marie Skłodowska-Curie Grant Agreement SELPH2D No. 839217. Work by F.G. was supported by the US Department of Energy (DOE), Office of Science, Basic Energy Sciences (BES) under Award No. DE-SC0020129.

[1] M. N. Ali, J. Xiong, S. Flynn, J. Tao, Q. D. Gibson, L. M. Schoop, T. Liang, N. Haldolaarachchige, M. Hirschberger, N. P. Ong, and R. J. Cava, Large, non-saturating magnetoresistance in WTe_2, Nature (London) **514**, 205 (2014).

[2] X. C. Pan, X. Chen, H. Liu, Y. Feng, Z. Wei, Y. Zhou, Z. Chi, L. Pi, F. Yen, F. Song, and X. Wan, Pressure-driven dome-shaped superconductivity and electronic structural evolution in tungsten ditelluride, Nat. Commun. **6**, 7805 (2015).

[3] D. Kang, Y. Zhou, W. Yi, C. Yang, J. Guo, Y. Shi, S. Zhang, Z. Wang, C. Zhang, S. Jiang, A. Li, K. Yang, Q. Wu, G. Zhang, L. Sun, and Z. Zhao, Superconductivity emerging from a suppressed large magnetoresistant state in tungsten ditelluride, Nat. Commun. **6**, 7804 (2015).

[4] D. H. Keum, S. Cho, J. H. Kim, D.-H. Choe, H.-J. Sung, M. Kan, H. Kang, J.-Y. Hwang, S. W. Kim, H. Yang, K. J. Chang, and Y. H. Lee, Bandgap opening in few-layered monoclinic $MoTe_2$, Nat. Phys. **11**, 482 (2015).

[5] S. Lee, J. Jang, S.-I. Kim, S.-G. Jung, J. Kim, S. Cho, S. W. Kim, J. Y. Rhee, K.-S. Park, and T. Park, Origin of extremely large magnetoresistance in the candidate type-II Weyl semimetal $MoTe_{2-x}$, Sci. Rep. **8**, 13937 (2018).

[6] S. Thirupathaiah, R. Jha, B. Pal, J. S. Matias, P. K. Das, P. K. Sivakumar, I. Vobornik, N. C. Plumb, M. Shi, R. A. Ribeiro, and D. D. Sarma, $MoTe_2$: An uncompensated semimetal with extremely large magnetoresistance, Phys. Rev. B **95**, 241105(R) (2017).

[7] Y. Qi, P. G. Naumov, M. N. Ali, C. R. Rajamathi, O. Barkalov, Y. Sun, C. Shekhar, S.-C. Wu, V. Süß, M. Schmidt, E. Pippel, P. Werner, R. Hillebrand, T. Förster, E. Kampertt, W. Schnelle, S. Parkin, R. J. Cava, C. Felser, B. Yan, and S. A. Medvedev, Superconductivity in Weyl semimetal candidate $MoTe_2$, Nat. Commun. **7**, 11038 (2016).

[8] H. Takahashi, T. Akiba, K. Imura, T. Shiino, K. Deguchi, N. K. Sato, H. Sakai, M. S. Bahramy, and S. Ishiwata, Anticorrelation between polar lattice instability and superconductivity in the Weyl semimetal candidate $MoTe_2$, Phys. Rev. B **95**, 100501(R) (2017).

[9] C. Heikes, I. Lin Liu, T. Metz, C. Eckberg, P. Neves, Y. Wu, L. Hung, P. Piccoli, H. Cao, J. Leao, J. Paglione, T. Yildirim, N. P. Butch, and W. Ratcliff, Mechanical control of crystal symmetry and superconductivity in Weyl semimetal $MoTe_2$, Phys. Rev. Mater. **2**, 074202 (2018).

[10] Z. Guguchia, F. von Rohr, Z. Shermadini, A. T. Lee, S. Banerjee, A. R. Wieteska, C. A. Marianetti, H. Luetkens, Z. Gong, B. A. Frandsen, S. C. Cheung, C. Baines, A. Shengelaya, A. N. Pasupathy, E. Morenzoni, S. J. L. Billinge, A. Amato, R. J. Cava, R. Khasanov, and Y. J. Uemura, Signatures of the topological s^{+-} superconducting order parameter in the type-II Weyl semimetal T_d-$MoTe_2$, Nat. Commun. **8**, 1082 (2017).

[11] S. Dissanayake, C. Duan, J. Yang, J. Liu, M. Matsuda, C. Yue, J. A. Schneeloch, J. C. Y. Teo, and D. Louca, Electronic band tuning under pressure in $MoTe_2$ topological semimetal, npj Quantum Mater. **4**, 45 (2019).

[12] Y. Sun, S. C. Wu, M. N. Ali, C. Felser, and B. Yan, Prediction of Weyl semimetal in orthorhombic $MoTe_2$, Phys. Rev. B **92**, 161107(R) (2015).

[13] A. A. Soluyanov, D. Gresch, Z. Wang, Q. Wu, M. Troyer, X. Dai, and B. A. Bernevig, Type-II Weyl semimetals, Nature (London) **527**, 495 (2015).

[14] Z. Wang, D. Gresch, A. A. Soluyanov, W. Xie, S. Kushwaha, X. Dai, M. Troyer, R. J. Cava, and B. A. Bernevig, $MoTe_2$: A Type-II Weyl Topological Metal, Phys. Rev. Lett. **117**, 056805 (2016).

[15] A. Tamai, Q. S. Wu, I. Cucchi, F. Y. Bruno, S. Riccò, T. K. Kim, M. Hoesch, C. Barreteau, E. Giannini, C. Besnard, A. A. Soluyanov, and F. Baumberger, Fermi Arcs and Their Topological Character in the Candidate Type-II Weyl Semimetal $MoTe_2$, Phys. Rev. X **6**, 031021 (2016).

[16] K. Deng, G. Wan, P. Deng, K. Zhang, S. Ding, E. Wang, M. Yan, H. Huang, H. Zhang, Z. Xu, J. Denlinger, A. Fedorov, H. Yang, W. Duan, H. Yao, Y. Wu, S. Fan, H. Zhang, X. Chen, and S. Zhou, Experimental observation of topological Fermi arcs in type-II Weyl semimetal $MoTe_2$, Nat. Phys. **12**, 1105 (2016).

[17] Y. Li, Q. Gu, C. Chen, J. Zhang, Q. Liu, X. Hu, J. Liu, Y. Liu, L. Ling, M. Tian, Y. Wang, N. Samarth, S. Li, T. Zhang, J. Feng, and J. Wang, Nontrivial superconductivity in topological $MoTe_{2-x}S_x$ crystals, Proc. Natl. Acad. Sci. USA **115**, 9503 (2018).

[18] X. Luo, F. C. Chen, J. L. Zhang, Q. L. Pei, G. T. Lin, W. J. Lu, Y. Y. Han, C. Y. Xi, W. H. Song, and Y. P. Sun, T_d-$MoTe_2$: A possible topological superconductor, Appl. Phys. Lett. **109**, 102601 (2016).

[19] Y. Naidyuk, O. Kvitnitskaya, D. Bashlakov, S. Aswartham, I. Morozov, I. Chernyavskii, G. Fuchs, S.-L. Drechsler, R. Hühne, K. Nielsch, B. Büchner, and D. Efremov, Surface superconductivity in the Weyl semimetal $MoTe_2$ detected by point contact spectroscopy, 2D Mater. **5**, 045014 (2018).

[20] P. Hosur, X. Dai, Z. Fang, and X.-L. Qi, Time-reversal-invariant topological superconductivity in doped Weyl semimetals, Phys. Rev. B **90**, 045130 (2014).

[21] F. C. Chen, X. Luo, R. C. Xiao, W. J. Lu, B. Zhang, H. X. Yang, J. Q. Li, Q. L. Pei, D. F. Shao, R. R. Zhang, L. S. Ling, C. Y. Xi, W. H. Song, and Y. P. Sun, Superconductivity enhancement in the S-doped Weyl semimetal candidate $MoTe_2$, Appl. Phys. Lett. **108**, 162601 (2016).

[22] M. Mandal, S. Marik, K. P. Sajilesh, Arushi, D. Singh, J. Chakraborty, N. Ganguli, and R. P. Singh, Enhancement of the superconducting transition temperature by Re doping in Weyl semimetal $MoTe_2$, Phys. Rev. Mater. **2**, 094201 (2018).

[23] S. Cho, S. H. Kang, H. S. Yu, H. W. Kim, W. Ko, S. W. Hwang, W. H. Han, D. H. Choe, Y. H. Jung, K. J. Chang, and Y. H. Lee, Te vacancy-driven superconductivity in orthorhombic molybdenum ditelluride, 2D Mater. **4**, 021030 (2017).

[24] P. Li, J. Cui, J. Zhou, D. Guo, J. Yi, Z. Zhao, J. Fan, Z. Ji, X. Jing, F. Qu, C. Yang, L. Lu, J. Lin, Z. Liu, and G. Liu, Phase transition and superconductivity enhancement in Se-substituted $MoTe_2$ thin films, Adv. Mater. **31**, 1904641 (2019).

[25] P. B. Allen and B. Mitrović, Theory of superconducting T_c, Solid State Phys. **37**, 1 (1983).

[26] E. R. Margine and F. Giustino, Anisotropic Migdal-Eliashberg theory using Wannier functions, Phys. Rev. B **87**, 024505 (2013).

[27] P. Giannozzi, O. Andreussi, T. Brumme, O. Bunau, M. B. Nardelli, M. Calandra, R. Car, C. Cavazzoni, D. Ceresoli, M. Cococcioni *et al.*, Advanced capabilities for materials modelling with QUANTUM ESPRESSO, J. Phys.: Condens. Matter **29**, 465901 (2017).

[28] E. Kucukbenli, M. Monni, B. I. Adetunji, X. Ge, G. A. Adebayo, N. Marzari, S. De Gironcoli, and A. Dal Corso, Projector augmented-wave and all-electron calculations across

the periodic table: A comparison of structural and energetic properties arXiv:1404.3015.

[29] J. P. Perdew, K. Burke, and M. Ernzerhof, Generalized Gradient Approximation Made Simple, Phys. Rev. Lett. **77**, 3865 (1996).

[30] J. Klimeš, D. R. Bowler, and A. Michaelides, van der Waals density functionals applied to solids, Phys. Rev. B **83**, 195131 (2011).

[31] J. Klimeš, D. R. Bowler, and A. Michaelides, Chemical accuracy for the van der Waals density functional, J. Phys.: Condens. Matter **22**, 022201 (2010).

[32] H. J. Monkhorst and J. D. Pack, Special points for Brillouin-zone integrations, Phys. Rev. B **13**, 5188 (1976).

[33] M. Methfessel and A. T. Paxton, High-precision sampling for Brillouin-zone integration in metals, Phys. Rev. B **40**, 3616 (1989).

[34] S. Baroni, S. de Gironcoli, A. Dal Corso, and P. Giannozzi, Phonons and related properties of extended systems from density-functional perturbation theory, Rev. Mod. Phys. **73**, 515 (2001).

[35] F. Giustino, M. L. Cohen, and S. G. Louie, Electron-phonon interaction using Wannier functions, Phys. Rev. B **76**, 165108 (2007).

[36] S. Poncé, E. R. Margine, C. Verdi, and F. Giustino, EPW: Electron-phonon coupling, transport and superconducting properties using maximally localized Wannier functions, Comput. Phys. Commun. **209**, 116 (2016).

[37] N. Marzari, A. A. Mostofi, J. R. Yates, I. Souza, and D. Vanderbilt, Maximally localized Wannier functions: Theory and applications, Rev. Mod. Phys. **84**, 1419 (2012).

[38] G. Pizzi, V. Vitale, R. Arita, S. Bluegel, F. Freimuth, G. Géranton, M. Gibertini, D. Gresch, C. Johnson, T. Koretsune *et al.*, Wannier90 as a community code: New features and applications, J. Phys.: Condens. Matter. **32**, 165902 (2019).

[39] B. E. Brown, The crystal structures of WTe_2 and high-temperature $MoTe_2$, Acta Crystallogr. **20**, 268 (1966).

[40] See Supplemental Material at http://link.aps.org/supplemental/10.1103/PhysRevB.101.214515 for further details on the first-principles calculations, Figs. S1– S11, and Table S1.

[41] K. Zhang, C. Bao, Q. Gu, X. Ren, H. Zhang, K. Deng, Y. Wu, Y. Li, J. Feng, and S. Zhou, Raman signatures of inversion symmetry breaking and structural phase transition in type-II Weyl semimetal $MoTe_2$, Nat. Commun. **7**, 13552 (2016).

[42] Q. Song, H. Wang, X. Pan, X. Xu, Y. Wang, Y. Li, F. Song, X. Wan, Y. Ye, and L. Dai, Anomalous in-plane anisotropic Raman response of monoclinic semimetal 1T′-$MoTe_2$, Sci. Rep. **7**, 1758 (2017).

[43] S. M. Oliver, R. Beams, S. Krylyuk, I. Kalish, A. K. Singh, A. Bruma, F. Tavazza, J. Joshi, I. R. Stone, S. J. Stranick, A. V Davydov, and P. M. Vora, The structural phases and vibrational properties of $Mo_{1-x}W_xTe_2$ alloys, 2D Mater. **4**, 045008 (2017).

[44] S.-Y. Chen, T. Goldstein, D. Venkataraman, A. Ramasubramaniam, and J. Yan, Activation of new Raman modes by inversion symmetry breaking in type II Weyl semimetal candidate T′-$MoTe_2$, Nano Lett. **16**, 5852 (2016).

[45] J. G. Si, W. J. Lu, H. Y. Lv, B. C. Zhao, and Y. P. Sun, Pressure controllable phase transition in $MoTe_2$ by the interlayer band occupancy, Phys. Lett. A **383**, 126016 (2019).

[46] P. Lu, J.-S. Kim, J. Yang, H. Gao, J. Wu, D. Shao, B. Li, D. Zhou, J. Sun, D. Akinwande, D. Xing, and J.-F. Lin, Origin of superconductivity in the Weyl semimetal WTe_2 under pressure, Phys. Rev. B **94**, 224512 (2016).

[47] K. Momma and F. Izumi, VESTA 3 for three-dimensional visualization of crystal, volumetric and morphology data, J. Appl. Crystallogr. **44**, 1272 (2011).

[48] J. Bardeen, L. N. Cooper, and J. R. Schrieffer, Theory of Superconductivity, Phys. Rev. **108**, 1175 (1957).

[49] D. Rhodes, R. Schönemann, N. Aryal, Q. Zhou, Q. R. Zhang, E. Kampert, Y.-C. Chiu, Y. Lai, Y. Shimura, G. T. McCandless, J. Y. Chan, D. W. Paley, J. Lee, A. D. Finke, J. P. C. Ruff, S. Das, E. Manousakis, and L. Balicas, Bulk Fermi surface of the Weyl type-II semimetallic candidate γ-$MoTe_2$, Phys. Rev. B **96**, 165134 (2017).

[50] M. Sakano, M. S. Bahramy, H. Tsuji, I. Araya, K. Ikeura, H. Sakai, S. Ishiwata, K. Yaji, K. Kuroda, A. Harasawa, S. Shin, and K. Ishizaka, Observation of spin-polarized bands and domain-dependent Fermi arcsin polar Weyl semimetal $MoTe_2$, Phys. Rev. B **95**, 121101(R) (2017).

[51] Q. Wu, S. Zhang, H.-F. Song, M. Troyer and A. A. Soluyanov, WannierTools: An open-source software package for novel topological materials, Comput. Phys. Commun. **224**, 405 (2018).

[52] J. Bekaert, E. Khestanova, D. G. Hopkinson, J. Birkbeck, N. Clark, M. Zhu, D. A. Bandurin, R. Gorbachev, S. Fairclough, Y. Zou, M. Hamer, D. J. Terry, J. J. P. Peters, A. M. Sanchez, B. Partoens, S. J. Haigh, M. V. Milošević, and I. V. Grigorieva, Enhanced superconductivity in few-layer TaS_2 due to healing by oxygenation, Nano. Lett. **20**, 3808 (2020).

[53] M. Leroux, I. Errea, M. Le Tacon, S.-M. Souliou, G. Garbarino, L. Cario, A. Bosak, F. Mauri, M. Calandra, and P. Rodiére, Strong anharmonicity induces quantum melting of charge density wave in 2*H*-$NbSe_2$ under pressure, Phys. Rev. B **92**, 140303(R) (2015).

[54] C. Heil, S. Poncé, H. Lambert, M. Schlipf, E. R. Margine, and F. Giustino, Origin of Superconductivity and Latent Charge Density Wave in NbS_2, Phys. Rev. Lett. **119**, 087003 (2017).

[55] M. Rösner, S. Haas, and T. O. Wehling, Phase diagram of electron-doped dichalcogenides, Phys. Rev. B **90**, 245105 (2014).

[56] T. Das and K. Dolui, Superconducting dome in MoS_2 and $TiSe_2$ generated by quasiparticle-phonon coupling, Phys. Rev. B **91**, 094510 (2015).

[57] J. Bekaert, A. Aperis, B. Partoens, P. M. Oppeneer, and M. V. Milošević, Advanced first-principles theory of superconductivity including both lattice vibrations and spin fluctuations: The case of FeB_4, Phys. Rev. B **97**, 014503 (2018).

[58] E. R. Margine, H. Lambert, and F. Giustino, Electron-phonon interaction and pairing mechanism in superconducting Ca-intercalated bilayer graphene, Sci. Rep. **6**, 21414 (2016).

[59] I. Errea, F. Belli, L. Monacelli, A. Sanna, T. Koretsune, T. Tadano, R. Bianco, M. Calandra, R. Arita, F. Mauri, and J. A. Flores-Livas, Quantum crystal structure in the 250-kelvin superconducting lanthanum hydride, Nature (London) **578**, 66 (2020).

[60] A. Sanna, J. A. Flores-Livas, A. Davydov, G. Profeta, K. Dewhurst, S. Sharma, and E. K. U. Gross, *Ab initio* Eliashberg theory: Making genuine predictions of superconducting features, J. Phys. Soc. Jpn. **87**, 041012 (2018).

[61] G. Marini, P. Barone, A. Sanna, C. Tresca, L. Benfatto, and G. Profeta, Superconductivity in tin selenide under pressure, Phys. Rev. Mater. **3**, 114803 (2019).

[62] B. Wiendlocha, R. Szcześniak, A. P. Durajski, and M. Muras, Pressure effects on the unconventional superconductivity of noncentrosymmetric $LaNiC_2$, Phys. Rev. B **94**, 134517 (2016).

[63] J. Towns, T. Cockerill, M. Dahan, I. Foster, K. Gaither, A. Grimshaw, V. Hazlewood, S. Lathrop, D. Lifka, G. D. Peterson, R. Roskies, J. R. Scott, and N. Wilkins-Diehr, XSEDE: Accelerating scientific discovery, Comput. Sci. Eng. **16**, 62 (2014).